ACS Catalysis

pubs.acs.org/acscatalysis

Research Article

Neutralization of Reactive Oxygen Species at Dinuclear Cu(II)-Cores: Tuning the Antioxidant Manifold in Water by Ligand Design

Andrea Squarcina, Alice Santoro, Neal Hickey, Rita De Zorzi, Mauro Carraro, Silvano Geremia, Marco Bortolus, Marilena Di Valentin, and Marcella Bonchio*

Cite This: *ACS Catal.* 2020, 10, 7295–7306

Read Online

ACCESS | Metrics & More | Article Recommendations | Supporting Information

ABSTRACT: Dinuclear Cu_2(II,II)-cores stabilized by the N_3O donorset of HL^1 = (2-{[[di(2-pyridyl)methyl](methyl)amino]methyl}phenol), HL^2 = 2-({[di(2-pyridyl)methyl]amino}methyl)phenol), and HL^3 = 2-({[di(2-pyridyl)methyl]amino}methyl)-4-nitrophenol display a unique superoxide dismutase (SOD) combined with catalase (CAT)-like activity in water, at neutral pH. The $\mathbf{Cu_2L^1_2}$ < $\mathbf{Cu_2L^2_2}$ < $\mathbf{Cu_2L^3_2}$ structure–reactivity trend puts a spotlight on the electron-deficient core of $\mathbf{Cu_2L^3_2}$ that exhibits the highest SOD (log $k_{cat}(O_2^{\bullet-})$ = 7.55) and CAT-like ($k_{H_2O_2}$ = 0.66 M^{-1} s^{-1}) performance. Time-lapse ESI-MS and EPR experiments indicate that a dimeric core is essential for oxygenic turnover upon H_2O_2 decomposition.

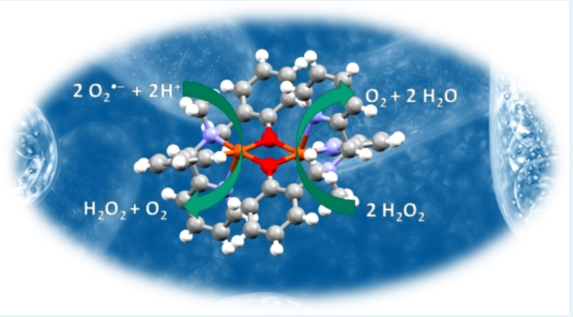

KEYWORDS: *artificial enzymes, copper catalysis, superoxide dismutase, catalase, antioxidant catalysis*

INTRODUCTION

O_2 multiredox chemistry is essential for aerobic life. On the other hand, processing of O_2 via multielectron transfer is also associated with the release of toxic radical species. These are generally defined as reactive oxygen species (ROS) and include the superoxide anion ($O_2^{\bullet-}$), hydrogen peroxide (H_2O_2), and the hydroxyl radical species (HO•). At the cellular level, ROS-specific enzymes provide the natural defense against this oxidative risk. The antioxidant frontline stems from the combined action of superoxide dismutase (Cu–Zn, Mn, Fe, Ni-dependent SOD), catalase (Fe, Mn-dependent catalase (CAT)), and glutathione peroxidase (GSX).[1,2] ROS detoxification occurs via a cascade catalysis initiated by SOD via $O_2^{\bullet-}$ dismutation to O_2 and H_2O_2, and terminated by CAT/GSH using hydrogen peroxide as the primary substrate. This enzymatic domino effect is instrumental to prevent H_2O_2 accumulation and the insurgence of branching radical chains, Haber–Weiss chemistry, responsible for an exponential increase of the oxidative risk.[1,2] Indeed, biorelevant metal ions, like Fe(II/III) or Cu(I/II), have been recently investigated in terms of their double-faceted antioxidant effect or toxicity as the two sides of the same coin. In particular the multisite binding modes and equilibria of copper ions at protein sites are being investigated with regard to cellular toxicity and disease pathogenesis.[3] Therefore, a new route can be traced by evaluating the Cu-induced risk based on the stereoelectronic features of copper sites that regulate the Cu-redox manifold and its response toward ROS generation/neutralization.[3]

In this respect, the natural copper–zinc superoxide dismutase (Cu–ZnSOD) shows a heterobimetallic active site, with a penta-coordinated Cu^{II} center ligated by four His residues and one water molecule with a distorted square pyramidal coordination geometry. During SOD turnover, the redox-active copper center cycles between the $Cu^{II/I}$ oxidation states upon interaction with $O_2^{\bullet-}$ (eqs 1 and 2), while zinc appears to play a role in the overall folding stability and in facilitating a broader pH independence.[4]

$$O_2^{\bullet-} + Cu^{II}–Zn^{II}SOD \rightarrow O_2 + Cu^{I}–Zn^{II}SOD \quad (1)$$

$$O_2^{\bullet-} + 2H^+ + Cu^{I}–Zn^{II}SOD \rightarrow H_2O_2 + Cu^{II}–Zn^{II}SOD \quad (2)$$

Due to the rich oxygen chemistry known for copper complexes, reduction to Cu(I) offers competing radical mechanisms by intercepting oxygen (eqs 3 and 4) and/or by single electron transfer to H_2O_2.[5]

$$Cu(I) + O_2 \rightarrow Cu(II)OO\bullet \quad (3)$$

$$Cu(I) + H_2O_2 \rightarrow Cu(II) + OH^- + \bullet OH \quad (4)$$

Received: May 1, 2020
Revised: May 12, 2020
Published: May 14, 2020

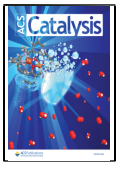

https://dx.doi.org/10.1021/acscatal.0c01955
ACS Catal. 2020, 10, 7295–7306

Table 1. Catalytic Copper Antioxidants Featuring SOD and CAT Activity in Water[a]

	E^b/mV vs NHE		SOD activity[c]	CAT activity[d]				
catalysts	$Cu_2^{II,II/I,I}$ ($E_{1/2}$)	$Cu_2^{III,III/II,II}$ (E_p)	log $k_{cat}(O_2^{\bullet-})$ (IC_{50}, μM)	R_{max} (μM O_2 s^{-1})	TON	$k_{H_2O_2}$ (M^{-1} s^{-1})	pH	ref
$Cu,Zn\text{-}SOD_{(human)}$	~+400		9.30 (~0.0013)				7.8	4
$Mn_2\text{-}CAT_{(T.thermophilus)}$				nd[e]	nd	3.1×10^6	7−10	11
$\mathbf{Cu_2L^1_2}$	−161	+1110	6.80 (0.40)	0.87[f]; 0.51[g]	52[f]; 110[g]	0.23[f]	7.8[f]; 7.4[g]	this work
$\mathbf{Cu_2L^2_2}$	−55	+1070	7.27 (0.14)	4.4[f]; 1.1[g]	60[f]; 110[g]	0.65[f]	7.8[f]; 7.4[g]	this work
$\mathbf{Cu_2L^3_2}$	+60	+1310	7.55 (0.072)	4.3[f]; 1.0[g]	60[f]; 110[g]	0.66[f]	7.8[f]; 7.4[g]	this work
$Cu(TAAP)(NO_3)_2$	+291	nd	7.26 (0.55)[h]	nd	nd	nd	7.0	10a
$[Cu(PBMPA)]^+$	−187	nd	7.09 (1.04)	14.4[i]	125[i]	0.030[i]	11.0	46
CuCyss	nd	nd	6.42 (9.90)	0.40[j]	nd	nd	7.4	10d
$[Cu(apz\text{-}pn)]^{2+}$	nd	nd	7.22 (0.090)[h]	nd	nd	1.10[i]	8.0	10c

[a]Ligand abbreviations are as follows: TAAP = obtained by self-condensation of 5-amino-3-methyl-l- phenylpyrazole-4-carbaldehyde (AMPC) in the presence of copper(II); HPBMPA = N-propanoate-*N*,*N*-bis(2-pyridylmethyl)amine; Cyss = cystine; apz-pn = *N*,*N*′-bis(2-acetylpyrazyl)methylene-1,3-diaminopropane. [b]$E_{1/2}$ is measured in 0.05 M phosphate buffer, pH 7.8, 0.1 M NaCl. [c]SOD activity based on the cyt c assay where radical anions are generated by the xanthine/xanthine oxidase system (40 μM xanthine, 0.0053 U mL^{-1} xanthine oxidase, 10 μM cyt c, catalase 15 μg mL^{-1}, 50 mM phosphate buffer, pH = 7.80). IC_{50} indicates the catalyst concentration required to attain 50% inhibition of the cyt c reduction; log $k_{cat}(O_2^{\bullet-})$ refers to the rate constant of catalytic superoxide dismutation; estimated errors are within ±10%. [d]CAT activity is based on oxygen evolution kinetics, monitored by a pressure transducer. R_{max} were obtained by linear regression of data within 10% H_2O_2 conversion; the estimated errors are within ±10%. $k_{H_2O_2}$ obtained by linear regression of pseudo-first-order rate constants $k_{obs} = k_{H_2O_2}[H_2O_2]$. [e]nd = not determined. [f]Measured in 50 mM BBS, pH 7.8 at 25 °C. [g]Measured in 50 mM KH buffer, pH 7.4 at 25 °C. [h]SOD activity is measured by NBT assay. [i]CAT activity is based on oxygen evolution kinetics, monitored by a reverse buret. [j]CAT activity is based on oxygen evolution kinetics, monitored by Warburg apparatus.

Scheme 1. Synthesis, Ligands, and X-ray Crystal Structures of $Cu_2L^1_2$, $Cu_2L^2_2$, and $Cu_2L^3_2$[a]

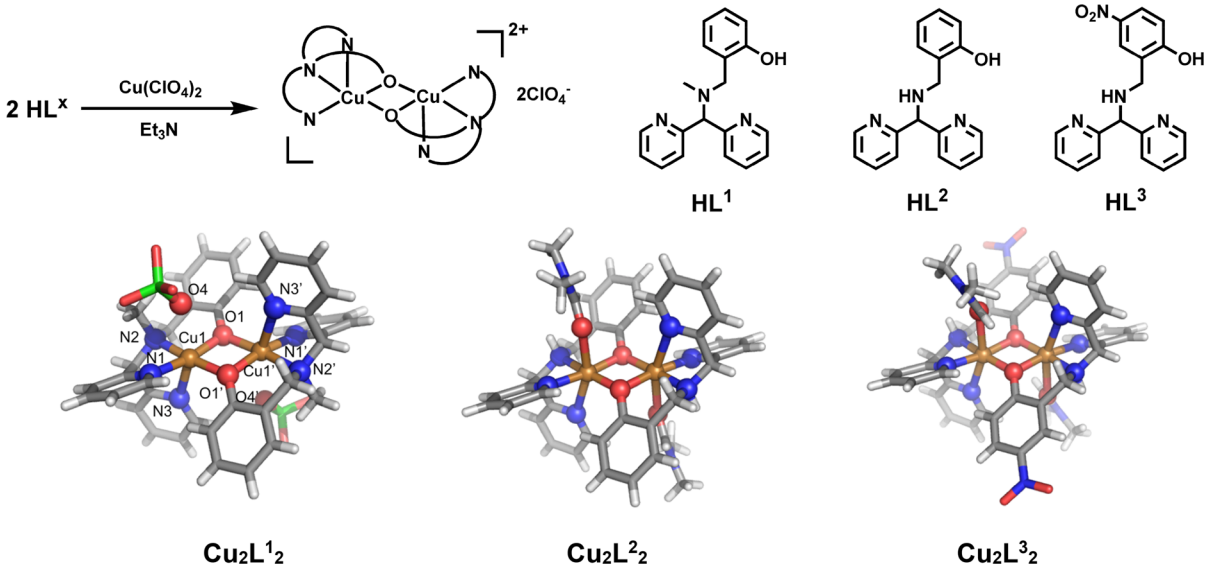

[a]For clarity, counter ions and solvent molecules which are not part of the Cu coordination spheres have been omitted.

The final outcome is the paradox of the enhanced toxicity registered within brain tissues when the isolated Cu−ZnSOD (bovine protein) is administered as antioxidant under anoxia/reoxygenation conditions.[6] This example highlights the crucial issue of designing a multilevel catalytic manifold that goes beyond a specific ROS target and works for the simultaneous neutralization of ROS cascades. We have recently reported on a Mn-based synthetic "di-zyme" behaving as the artificial SOD/CAT conjugate with the highest activity reported up to date for a Mn catalyst.[7] In the case of copper species, the majority of SOD-mimetics display a mononuclear Cu(II) center and generally fail to provide a bielectronic mechanism for H_2O_2 dismutation.[8,9] Few single-site Cu(II)-complexes are reported to exhibit a dual SOD/CAT-like activity, while they were found to promote single-electron transfer mechanisms with the formation of harmful radical species (Table 1).[10] Dinuclear copper complexes, mimicking the structural motif of the manganese catalase, are known; however, their CAT-like activity has been reported only in organic solvents, lacking the complementary SOD-like functionality, and no examples of dual SOD/CAT dinuclear systems in water are known to date.[11,12]

Our results address the synthesis, solution, and solid state characterization of three novel Cu(II)-complexes, featuring a dinuclear copper-core stabilized by an N_3O donor ligand set (Scheme 1) and optimized for a combined superoxide dismutase and catalase-like activity in aqueous media, under physiological-like conditions. We show herein that the

https://dx.doi.org/10.1021/acscatal.0c01955
ACS Catal. 2020, 10, 7295−7306

stereoelectronic modulation of the Cu_2-coordination sphere is instrumental to tune the mechanism and the antioxidant performance of the resulting complexes. Finally insights on the evolution of the active species are discussed.

RESULTS AND DISCUSSION

Synthesis of Dinuclear Cu(II)-Complexes. The ligand HL^1 (2-{[[di(2-pyridyl)methyl](methyl)amino]methyl}-phenol) has been used to provide a tetradentate N_3O donor set for Cu(II) binding with a bis-pyridyl, tertiary amine, and phenolate terminals.[7,13] Ligand modification has been addressed with the 2-fold aim of implementing (i) accessibility of the catalytic core by using a nonmethylated, secondary amine binding site (HL^2 = 2-({[di(2-pyridyl)methyl]amino}-methyl)phenol); and (ii) a more electron-deficient copper-core by using *p*-nitrophenolate ligands (HL^3 = 2-({[di(2-pyridyl)-methyl]amino}methyl)-4-nitrophenol).[14] In all cases, dimeric $\mathbf{Cu_2L^x_2}$ complexes have been obtained by reacting the proper ligand HL^x with copper perchlorate and triethylamine in alcoholic solvents under reflux conditions (Scheme 1).[7,13] Green crystals suitable for X-ray analysis have been isolated upon addition of acetonitrile ($\mathbf{Cu_2L^1_2}$) or dimethylformamide (DMF) ($\mathbf{Cu_2L^2_2}$ and $\mathbf{Cu_2L^3_2}$) and cooling.[14]

X-ray Analysis. X-ray analysis of $\mathbf{Cu_2L^x_2}$ shows a C_i point-group symmetry for all three dinuclear complexes with a distorted octahedral geometry for the metal centers. Each Cu(II) atom is coordinated in a facial configuration by the three N atoms of the tetradentate ligand, while the phenolate ligands act as a bridge between the two metal centers. The metal coordination sphere is completed by a perchlorate ion in the $\mathbf{Cu_2L^1_2}$ structure and by a DMF molecule in the $\mathbf{Cu_2L^2_2}$ and $\mathbf{Cu_2L^3_2}$ structures (Scheme 1). From the crystallographic structures, minor differences are observed in the Cu_2O_2 core across the three complexes: the Cu−Cu distance ranges from 3.007 Å for $\mathbf{Cu_2L^1_2}$ to 3.033 Å for $\mathbf{Cu_2L^3_2}$ while the Cu−O−Cu angles slightly decrease, with values of 100.2° for $\mathbf{Cu_2L^1_2}$ and 99.9° for $\mathbf{Cu_2L^2_2}$ and $\mathbf{Cu_2L^3_2}$. The key feature observed moving from $\mathbf{Cu_2L^1_2}$ to $\mathbf{Cu_2L^2_2}$ or $\mathbf{Cu_2L^3_2}$, both bearing a secondary amine on the equatorial copper position, is the different accessibility of the metal centers due to the Jahn−Teller distortion, which results in a relative strong coordination of a solvent molecule (DMF) for these two complexes. Indeed, solvent coordination induces a remarkable elongation of the Cu−N3 binding motif (binding with the apical pyridine) from a value of 2.327 Å in the $\mathbf{Cu_2L^1_2}$ complex to 2.525 Å in the $\mathbf{Cu_2L^2_2}$ complex and 2.438 Å in the $\mathbf{Cu_2L^3_2}$ complex. This feature should impact on the substrate access to the copper active site and be relevant for catalysis (see structural parameters in the Supporting Information).

Spectroscopic and Solution Mass Characterization of the $\mathbf{Cu_2L^x_2}$ Complexes. The FT-IR spectra of the $\mathbf{Cu_2L^x_2}$ complexes confirm the ligand coordination mode, as the pyridines and phenol absorption bands are shifted toward higher frequencies upon metal binding and found at 1615−1600 cm^{-1} (Figures S11, S12, and S14).[15] The retention of the dinuclear structure in solution is confirmed by ESI-MS, UV−vis, and EPR analysis. In all cases, ESI(+)-MS peaks are obtained for the expected molecular ions as formate or perchlorate adducts (Table S3, formic acid was present in the eluent) with m/z = 779.0 $[\mathbf{Cu_2L^1_2} + HCO_2]^+$ and 833.0 $[\mathbf{Cu_2L^1_2} + ClO_4]^+$ (Figures S33 and S35); m/z = 751.0 $[\mathbf{Cu_2L^2_2} + HCO_2]^+$ and 805.0 $[\mathbf{Cu_2L^2_2} + ClO_4]^+$ (Figures S41 and S42); and m/z = 841.2 $[\mathbf{Cu_2L^3_2} + HCO_2]^+$ and 895.1 $[\mathbf{Cu_2L^3_2} + ClO_4]^+$ (Figures S43 and S44).[16]

Similar UV−vis spectra are collected for $\mathbf{Cu_2L^1_2}$, $\mathbf{Cu_2L^2_2}$, and $\mathbf{Cu_2L^3_2}$ (50−70 μM) both in organic (CH_3CN) and in aqueous phase (PBS 50 mM, pH 7.8) (Figures S3, S7, and S8). In particular, the absorption maximum at about 265 nm is ascribed to the $\pi-\pi^*$ transition of pyridines, while the phenolate ligand-to-metal charge transfer band is observed at higher wavelengths for $\mathbf{Cu_2L^1_2}$ at 410 nm (LMCT, ε = 1300 M^{-1} cm^{-1}), for $\mathbf{Cu_2L^2_2}$ at 397 nm (LMCT, ε = 1700 M^{-1} cm^{-1}), and for $\mathbf{Cu_2L^3_2}$ at 376 nm, overlapped with the absorption of the nitrophenol itself (ε = 23 000 M^{-1} cm^{-1}) (Figures S4, S6, and S8).[17] A d−d transition was also observed at 675 nm (ε = 280 M^{-1} cm^{-1}) for $\mathbf{Cu_2L^1_2}$, 668 nm (ε = 290 M^{-1} cm^{-1}) for $\mathbf{Cu_2L^2_2}$ and 670 nm (ε = 170 M^{-1} cm^{-1}) for $\mathbf{Cu_2L^3_2}$ (Figures S4, S7, and S8). These spectral features are in agreement with phenol deprotonation upon binding.[18] Moreover, the X-band EPR solution spectra are silent for all the complexes under investigation, thus confirming the stability of the dimeric core in aqueous phase (see further discussion, Figure 4, and Figure S76).

Electrochemistry. The redox properties of $\mathbf{Cu_2L^x_2}$ (0.5−1.0 mM) have been addressed by cyclic voltammetry (CV) experiments, performed both in acetonitrile and in aqueous solution (phosphate buffer, 50 mM, pH = 7.8). Under reductive scan in acetonitrile, one irreversible wave is attributed to the $Cu_2^{II,II/I,I}$ redox couple and observed at E_c = −136 mV (vs NHE) for $\mathbf{Cu_2L^1_2}$, while two irreversible waves are observed for the $Cu_2^{II,II/II,I}$ and $Cu_2^{II,I/I,I}$ redox couples at E^1_c = −96 mV and E^2_c = −465 mV, and at E^1_c = 62 mV and E^2_c = −273 mV (vs NHE), respectively, for $\mathbf{Cu_2L^2_2}$ and $\mathbf{Cu_2L^3_2}$ (Figures S16, S22, and S28). In aqueous media the corresponding redox processes display quasireversible features observed at $E_{1/2}$ = −161 (ΔE_p = 350 mV), −55 (ΔE_p = 116 mV), and 60 mV (ΔE_p = 450 mV) (vs NHE), respectively, for $\mathbf{Cu_2L^1_2}$, $\mathbf{Cu_2L^2_2}$, and $\mathbf{Cu_2L^3_2}$ species (see Table 1 and Figures S17, S23, and S29). The observed ΔE_p is likely ascribable to structural changes occurring for complex geometry upon oxidation and reduction of the copper-core. The increase of the potential values in the series indicates that the reduction of the copper-core is favored by less electron-donating ligands, that is, by replacing the tertiary amine in L^1 with a secondary amine in L^2 and by introducing the nitro-substituted phenolate in L^3.

In the oxidative scan in acetonitrile, two irreversible waves are tentatively attributed to the $Cu_2^{II,II} \rightarrow Cu_2^{III,II}$ and to the $Cu_2^{III,II} \rightarrow Cu_2^{III,III}$ processes, observed at E^1_a = 1.06 V and E^2_a = 1.38 V for $\mathbf{Cu_2L^1_2}$ (Figure S18), and at E^1_a = 1.28 V and E^2_a = 1.62 V for $\mathbf{Cu_2L^2_2}$ (Figure S24). A single wave is instead obtained at E^1_a = 1.56 V for $\mathbf{Cu_2L^3_2}$ (Figure S30).[19] In all cases, the addition of water yields the collapsing of the two anodic peaks into one single feature, observed at lower potential values (Figures S19, S25, and S31). Therefore, in aqueous phase, the proposed oxidation of the copper-core, $Cu_2^{II,II} \rightarrow Cu_2^{III,III}$, gives rise to an irreversible single wave observed at E_a = 1.11, 1.07, and 1.31 V (vs NHE) for $\mathbf{Cu_2L^1_2}$, $\mathbf{Cu_2L^2_2}$, and $\mathbf{Cu_2L^3_2}$ (Table 1, Figures S20, S26, and S32), likely implying a major structural change of the dinuclear complexes upon oxidation of the copper-core.[19,20] As expected, the NO_2-substituent effect in HL^3 is responsible for the increase of the oxidation potential observed for $\mathbf{Cu_2L^3_2}$. In all cases, oxidation of the phenolate moiety of the ligand is observed above 1.6 V.[21]

https://dx.doi.org/10.1021/acscatal.0c01955
ACS Catal. 2020, 10, 7295−7306

SOD-like Activity. Metal-based artificial SODs are initially assessed on the basis of the thermodynamic driving force available for both the oxidation and the reduction of the superoxide anion. This is readily measured by considering the redox potential of the catalytic manifold. A favorable potential range lies between the potentials for $O_2^{\bullet-}$ reduction to peroxide (0.89 V vs NHE, pH = 7) and its oxidation to O_2 (−0.16 V vs NHE, pH = 7), with the optimal value, considering outersphere electron transfer, being at E = 0.36 V (vs NHE).[5,22] Accordingly, all three complexes under investigation display the $Cu_2^{II,II/I,I}$ redox couple within the SOD potential range, with $\mathbf{Cu_2L^1_2}$ set at the lower limit (Table 1), while the redox placement of $\mathbf{Cu_2L^2_2}$ and $\mathbf{Cu_2L^3_2}$ is shifted toward the envisaged optimum, at E = 0.36 V vs NHE (Table 1).

The SOD-like activity of $\mathbf{Cu_2L^1_2}$, $\mathbf{Cu_2L^2_2}$, and $\mathbf{Cu_2L^3_2}$ has been screened with the xanthine oxidase/cytochrome c (cyt c) protocol to evaluate the $O_2^{\bullet-}$ scavenging efficiency, by comparing the IC_{50} performance (i.e., the catalyst concentration to achieve the 50% inhibition of cyt c reduction, monitored at 550 nm in 0.05 M phosphate buffer, pH 7.8) and the related kinetic constant ($\log k_{cat}(O_2^{\bullet-})$) (see the Supporting Information).[23]

Inspection of Table 1 results indicates that all three dicopper complexes work as artificial SODs in phosphate buffer (pH 7.8) following a clear structure−reactivity trend where $\mathbf{Cu_2L^1_2}$ < $\mathbf{Cu_2L^2_2}$ < $\mathbf{Cu_2L^3_2}$. In particular a steady increase of the log $k_{cat}(O_2^{\bullet-})$ values is observed in the series, (respectively, 6.80, 7.27, and 7.55, Table 1) corresponding to a parallel decrease of the IC_{50} concentration requirements, as low as 0.072 μM for $\mathbf{Cu_2L^3_2}$. This latter complex not only outperforms the related analogues but also stands as the most efficient Cu-based artificial SOD compared to either mono- or dinuclear literature benchmarks (Table 1).[8−10,24] The superior SOD-activity of $\mathbf{Cu_2L^3_2}$ is likely ascribed to the interplay of both thermodynamic and kinetic factors, as the nitro-substituted ligand HL^3 improves the electron acceptor properties of the copper-core ($E_{1/2}$ = 60 mV vs NHE, Table 1), while the secondary terminal amine can drive a favorable proton-coupled electron transfer (PCET) mechanism. In particular, the dependence of the SOD-like efficiency on the $Cu^{II/I}$ redox couple suggests a copper-mediated mechanism where the stereoelectronic features of the N_3O ligand set can provide (i) a prompt evolution/stabilization of the $Cu^{II/I}$ redox-manifold; (ii) an electrophilic and accessible recognition/binding site for $O_2^{\bullet-}$; and (iii) proximal hydrogen bonding donors/acceptors to drive favorable PCET mechanisms and the stabilization of peroxide intermediates.[8−10,22,24] While further studies are needed to clarify the role and impact of each effector to the catalytic activity, inspection of SOD performance suggests an innersphere dismutation reaction occurring at the single copper site (eqs 5 and 6).

$$O_2^{\bullet-} + Cu_2^{II,II}L_2 \rightarrow O_2 + Cu_2^{II,I}L_2 \quad (5)$$

$$O_2^{\bullet-} + 2H^+ + Cu_2^{II,I}L_2 \rightarrow H_2O_2 + Cu_2^{II,II}L_2 \quad (6)$$

According to this hypothesis, the copper site can cycle between a five to six coordinate coordination geometry during SOD catalysis (see the discussion in the X-ray Analysis section).

While catalytic dismutation of superoxide by $\mathbf{Cu_2L_2}$ is effective in the aqueous phase, oxidative degradation of the ligand dominates in CH_3CN and DMF even at low temperature (up to −80 °C), which hampers the detection of Cu-based superoxide and peroxide intermediates, generally characterized by distinct absorbance features at λ > 400 nm (ε = 10^3−10^4).[25,26]

CAT-like Activity. Copper-based artificial catalases, i.e., Cu-cores mimicking the inorganic cofactors of the natural catalases, are rare if compared with manganese or iron analogues.[2b,10] Expanding the copper role to H_2O_2 dismutation has the 2-fold aim of (i) implementing a dual SOD/CAT domino catalysis and (ii) understanding the stereoelectronic requirements to tune the reactivity at synthetic Cu-cores. This knowledge would stimulate new progress in the design of copper chelators that can revert the severe Cu-induced toxicity to a favorable and benign antioxidant effect.[27]

Enzymatic H_2O_2 dismutation involves a bielectronic process where both H_2O_2 reduction to H_2O and oxidation to O_2 are part of the catalytic turnover and occur with redox potential $E_{(O_2/H_2O_2)}$ = +0.28 and $E_{(H_2O_2/H_2O)}$ = +1.35 V (vs NHE, pH 7). In this scenario, the dicopper-core of $\mathbf{Cu_2L^x_2}$ is expected to cycle between the $Cu_2^{III,III}$ → $Cu_2^{II,II}$ redox manifold, via a bielectronic process and redox potentials falling in the range $E_{1/2}$ = 1.07−1.31 V (vs NHE, Table 1).[2b] The CAT activity of the $\mathbf{Cu_2L^x_2}$ was tested upon incubation with H_2O_2 (30 mM) in aqueous borate buffer (BBS, pH= 7.8) at 25 °C by monitoring the O_2 production kinetics with pressure transducer equipment (Figure 1 and the Supporting Information). The artificial catalase performance can be compared in terms of the O_2 evolution rate (R_{max}), the resulting H_2O_2 conversion (% yield), the turnover number (TON), and the second-order rate constant ($k_{H_2O_2}$, M^{-1} s^{-1}), determined under pseudo-first-order conditions, by varying the initial H_2O_2 concentration (Table 1 and the Supporting Information).[28] While in all cases, O_2 evolution levels off at ca. 35−40% yield (TON up to 60, Table 1), a 5-fold rate acceleration is observed by $\mathbf{Cu_2L^2_2}$ and $\mathbf{Cu_2L^3_2}$ as compared to $\mathbf{Cu_2L^1_2}$, with R_{max} = 4.4, 4.3, and 0.87 μM O_2 s^{-1}, respectively (Table 1). Moreover, oxygen evolution by $\mathbf{Cu_2L^1_2}$ occurs with a definite lag-time (ca. 10 min), that is absent in both $\mathbf{Cu_2L^2_2}$ and $\mathbf{Cu_2L^3_2}$ catalytic profiles (Figure 1). Inspection of data in Table 1 shows that such a ligand effect is not directly ascribed to the $Cu_2^{III,III}$ → $Cu_2^{II,II}$ redox potential and should be related to the more accessible and more flexible binding site of $\mathbf{Cu_2L^2_2}$ and $\mathbf{Cu_2L^3_2}$ lacking the steric hindrance

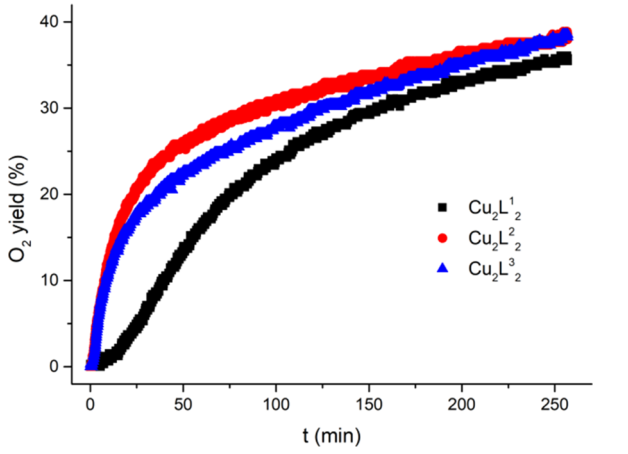

Figure 1. Comparison of O_2 evolution kinetics by $Cu_2L^1_2$, $Cu_2L^2_2$, and $Cu_2L^3_2$ (200 μM) upon incubation with H_2O_2 (30 mM) in BBS (50 mM pH = 7.8).

https://dx.doi.org/10.1021/acscatal.0c01955
ACS Catal. 2020, 10, 7295−7306

of the methylated tertiary amine (see the X-ray discussion and Supporting Information).[24]

It is noteworthy that, for all catalysts, the final O_2 production yield is increased up to 75% based on H_2O_2 conversion, TON = 110 (Table 1), in the Krebs–Henseleit buffer (KH buffer, pH = 7.4, commonly used in perfused and superfused solution protocols), that contains a mixture of salts (sulfates, phosphates, carbonates, and chlorides) and glucose (Figures S57 and S59).[7,29] However, in KH buffer, the O_2 evolution kinetics displays a lag-phase of ca. 10 min for $\mathbf{Cu_2L^2_2}$ and $\mathbf{Cu_2L^3_2}$, up to 100 min for $\mathbf{Cu_2L^1_2}$, and lower rates up to 1.1 μM O_2 s^{-1} (Table 1). This observation is consistent with possible inhibition by buffer anions (i.e., phosphate binding) that can slow down the overall process both in its initial phase and under turnover regime.[30,31]

Spectroscopic and Mechanistic Investigation of the CAT-like Reactivity by $\mathbf{Cu_2L^x_2}$. H_2O_2 dismutation by $\mathbf{Cu_2L^x_2}$ has been analyzed in more detail in order to address (i) the origin of the kinetic lag-phase, (ii) the evolution of the dicopper-core under the turnover regime, and (iii) the optimization of the catalytic efficiency. To this aim, time-dependent UV–vis, EPR, and ESI-MS evidence has been collected in acetonitrile and/or in aqueous BBS.[32]

In acetonitrile, under the conditions explored, the reference $\mathbf{Cu_2L^1_2}$ does not show any relevant CAT-activity, and no oxygen evolution is observed (Figure S61). On the contrary, addition of H_2O_2 (30 mM) to $\mathbf{Cu_2L^1_2}$ (200 μM in CH_3CN) causes a progressive modification of the UV–vis spectrum, with a decrease of the complex LMCT band at 410 nm, due to the Cu–phenolate interaction, and of the d–d bands at 675 nm, with the formation of three isosbestic points at 361, 475, and 612 nm (Figure 2a). This behavior is ascribed to a steady ligand degradation with bleaching of the copper-core features.

Indeed, ESI-MS analysis of the catalytic reaction shows a sharp decrease of the parent $\mathbf{Cu_2L^1_2}$ signals with a parallel formation of few low intensity peaks with m/z between 700 and 800 (Figures S34 and S62). In aqueous phase, under oxygen evolution conditions (BBS, 50 mM, pH 7.8), the UV–vis spectra collected over time (Figure 2b) show an initial shift of the LMCT and of the d–d bands to lower wavelengths (<20 min) followed by their progressive fading, with no clear isosbestic points. This behavior points to a stepwise evolution of the dinuclear copper-core and of the ligand environment, via the formation of definite copper-based intermediates, upon reaction with H_2O_2. Time-lapse ESI(+)-MS analysis is instrumental to identify the copper complexes generated along the reaction progress (Scheme 2, Figure 3, and Table S3). In particular, the parent $\mathbf{Cu_2L^1_2}$ (**1**), revealed at m/z = 751.0, 779.0, and 833.0 (see attribution in Table S3), is gradually converted to new dinuclear species (**2**), detected at a lower m/z ratio as a consequence of ligand oxidation, followed by the release of copper monomers (**3**), (Scheme 2, Table S3).[26] In particular, oxidation at the benzylic sites and cleavage of the resulting amidic bond are expected to yield ligand $\mathbf{L^{Ox}}$ and ligand $\mathbf{L^{Cl}}$ (inset box of Scheme 2).[33] The corresponding copper complexes are observed at m/z = 657.0 and 384.0 attributed, respectively, to dinuclear $[\mathbf{Cu_2L^{Ox}L^{Cl}}(O)]^+$ and to the monomer $[\mathbf{CuL^1}(OH)]^+$, formed in BBS solution, upon addition of H_2O_2, under oxygenic turnover (Scheme 2, Table S3).

Formation of monomers (**3**) shows a typical sigmoidal profile and levels off after ca. 150 min, at which point oxygen evolution slows down, and the reaction stops at ca. 40% yield.

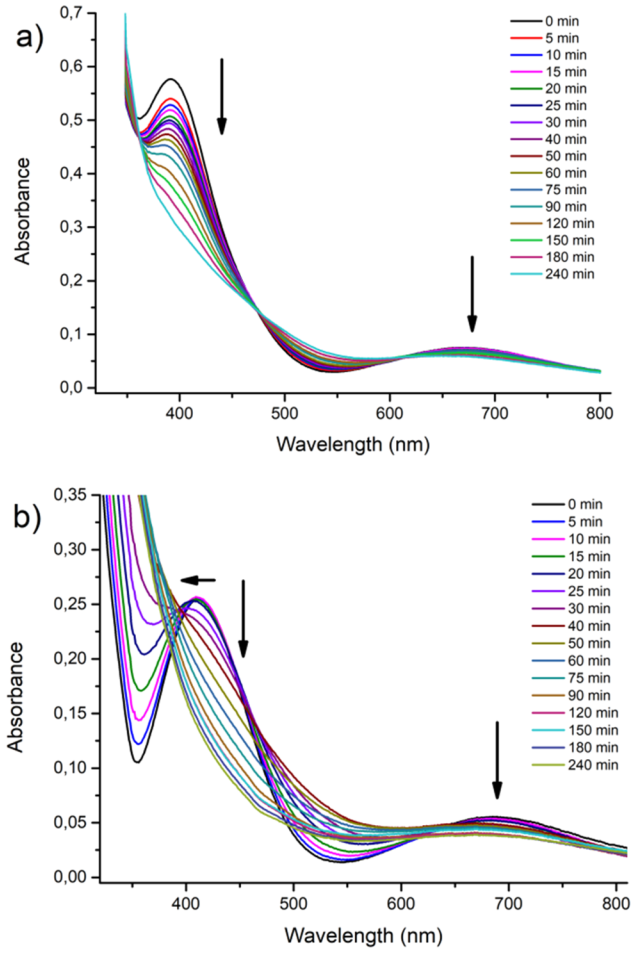

Figure 2. UV–vis spectra over time of the reaction ($[\mathbf{Cu_2L^1_2}]$ = 200 μM, $[H_2O_2]$ = 30 mM) in (a) acetonitrile and (b) BBS 50 mM pH = 7.8 (t = 0 min, before H_2O_2 addition).

Scheme 2. ESI(+)-MS Mapping of $\mathbf{Cu_2L^1_2}$ Evolution in the Presence of H_2O_2, Showing Ligand Oxidation (Inset Box) and Formation of Inactive Cu Monomers (Table S3)

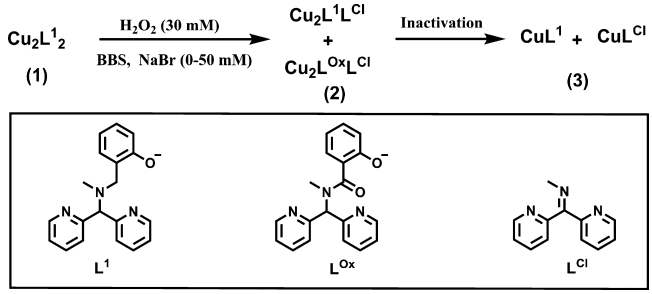

According to this scheme, the dicopper-cores of **1** and **2** are both active catalysts and display similar CAT-like activity, as no depletion of the oxygen production rate is observed at <50 min, where **1** is substantially converted into **2**, but **3** is still lagging behind. Along these lines, we can conclude that degradation of the dicopper-core of **1** and **2** to a single-site catalyst **3** is responsible for switching off H_2O_2 dismutation at >50 min. The monomeric form **3** is likely unable to mediate a bielectronic mechanism, despite standing as a barrier to prevent the release of ligand-free copper ions and the formation of copper oxides/hydroxides known to induce the

https://dx.doi.org/10.1021/acscatal.0c01955
ACS Catal. 2020, 10, 7295–7306

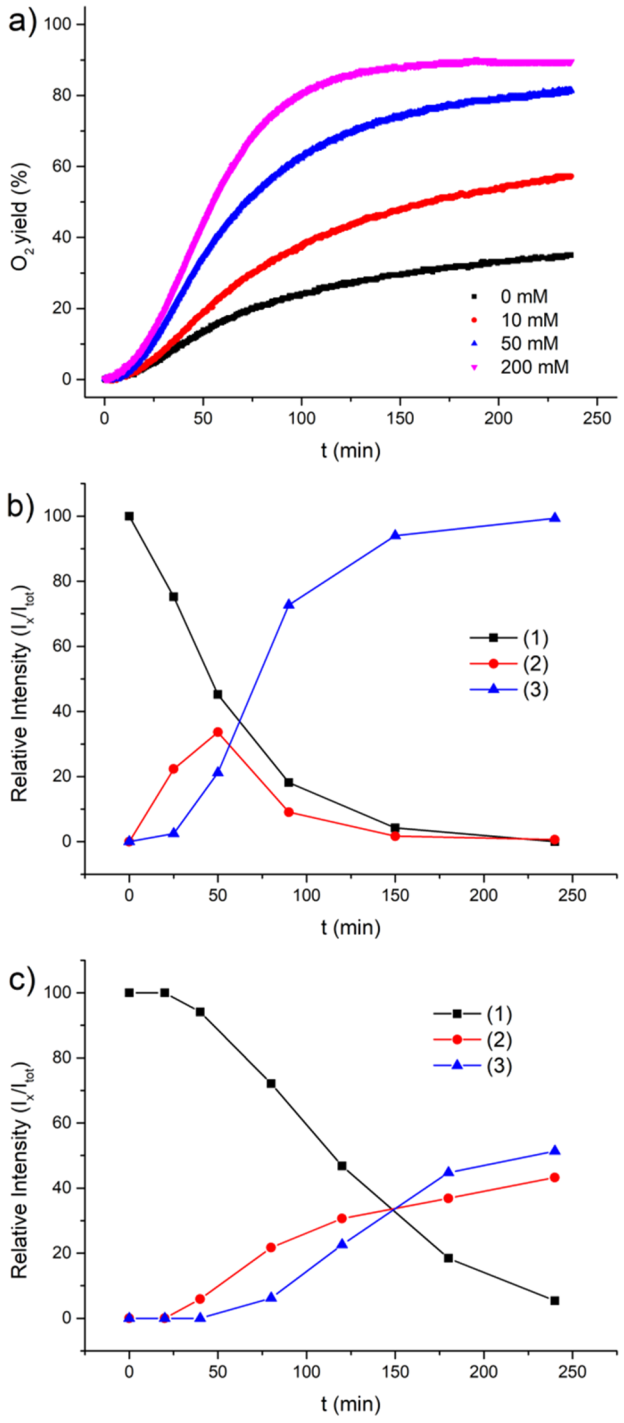

Figure 3. (a) O_2 evolution kinetics by $\mathbf{Cu_2L^1_2}$ (200 μM) upon incubation with H_2O_2 (30 mM) at 25 °C in BBS (50 mM pH = 7.8) with different concentration of NaBr. Catalyst evolution during the catalase cycle ([$\mathbf{Cu_2L^1_2}$] = 200 μM, [H_2O_2] = 30 mM in BBS 50 mM) monitored by ESI(+)-MS without (b) and in the presence of (c) [NaBr] = 50 mM where I_1 is associated with [(**1**)] (751.0 *m*/*z*, 779.0 *m*/*z*, 813.0 *m*/*z*, and 833.0 *m*/*z*), I_2 to [(**2**)] (657.0 *m*/*z* and 784.9 *m*/*z*), and I_3 to [(**3**)] 384.0 and 420.9 *m*/*z*) peaks intensity (Table S3). The relative amount of the specie (I_x/I_{tot}) was measured as the ratio between the intensity of the peaks attributed to a species (I_x) over the total species amount ($I_{tot} = I_1 + I_2 + I_3$). A similar behavior is obtained in the presence of NaBr, used as the scavenger of hydroxyl radicals (see further discussion), where additional peaks are observed at *m*/*z* = 784.9 and 420.9 attributed, respectively, to dinuclear [$\mathbf{Cu_2L^1L^{Cl}}$ + 2Br]$^+$ and to the monomer [$\mathbf{CuL^{Cl}}$ + Br]$^+$, (Scheme 2, Table S3). In order to trace the role of the different copper-complexes formed during turnover regime, the kinetic profile associated with species **1**−**3** (Scheme 2) was monitored in BBS (50 mM, pH 7.8) by ESI(+)-MS analysis and compared with the O_2 evolution kinetics (this figure). Interestingly, the catalyst transformation follows a consecutive reaction scheme, where the dinuclear complexes, **2**, originating from the pristine catalyst **1**, build up to a maximum after ca. 50 min and are consumed to yield monomers **3** (part b).

peroxide decomposition via radical-type mechanisms.[34] In order to inhibit possible Fenton-like radical reactions, NaBr was added at different concentrations, and the resulting oxygen evolution kinetics are reported in Figure 3a.[35] The reaction was carried out in aqueous phase (BBS 50 mM, pH 7.8) with the same catalyst concentration ($\mathbf{Cu_2L^1_2}$ = 200 μM) and NaBr in the range 10−200 mM (red, blue, and magenta curves in Figure 3a).

While there is no effect on the induction time of the reaction kinetics (Figure S64), meaning that no radical processes are involved in the initial catalyst activation, a remarkable enhancement of the oxygen evolution rate is obtained by increasing the NaBr concentration, which leads up to a 90% yield of oxygen production and TON = 134 (Table 2 and Figure 3a). Control experiments confirm that a minor pathway of oxygen evolution occurs by a parallel process involving the copper-free NaBr/H_2O_2 system (Figure S63). These observations indicate a prevalent CAT-like mechanism for O_2 production, while a parallel route of hydrogen peroxide degradation via a radical process and ligand oxidation is limited to ca. 10%.[36] These experiments may explain the increased performance registered in KH buffer, containing chloride and bicarbonate ions, likely serving as •OH radical scavengers (Table 1, Figures S57 and S59).[37] To investigate the effect of NaBr (50 mM) on the catalyst fate and lifespan, ESI(+)-MS analysis was performed during the reaction progress (blue line kinetics in Figure 3a,c). In this case, the degradation of the pristine catalyst **1** is stopped for ca. 30 min and then proceeds forming dinuclear **2**, and monomers **3** at a slower rate (compared in Figure 3b,c, see Scheme 2 and Table S3 for ESI(+)-MS data).

The NaBr effect translates into a longer-lived resting state of the active catalytic manifold (**1** + **2**) that is maintained for >100 min, thus sustaining the oxygen production rate and leading up to ca. 90% H_2O_2 conversion (Figure 3a, Table 2). In this scenario, the increase of rate and TON obtained in the

Table 2. Dependence of the Reaction Rate of O_2 Evolution by $\mathbf{Cu_2L^1_2}$ (200 μM) in the Presence of NaBr in BBS (50 mM, pH 7.8) and H_2O_2 (30 mM)[a]

[NaBr] (mM)	R_{max} (μM O_2 s^{-1})	TON	yield (%)
0	0.87	52	35
10	1.4	87	58
50	2.5	122	80
200	3.1	134	90

[a]Oxygen evolution kinetics monitored by a pressure transducer; R_{max} values were obtained by linear regression of data within 10% H_2O_2 conversion, and the estimated errors are within ±10%; yields based on H_2O_2 conversion; slight overestimation of TON values might depend on the side reaction occurring between Br^- and H_2O_2 (see Figure S63).

https://dx.doi.org/10.1021/acscatal.0c01955
ACS Catal. 2020, 10, 7295−7306

Scheme 3. Proposed Catalytic Cycle and Catalyst Evolution Occurring during H_2O_2 Dismutation by $Cu_2L^x_2$

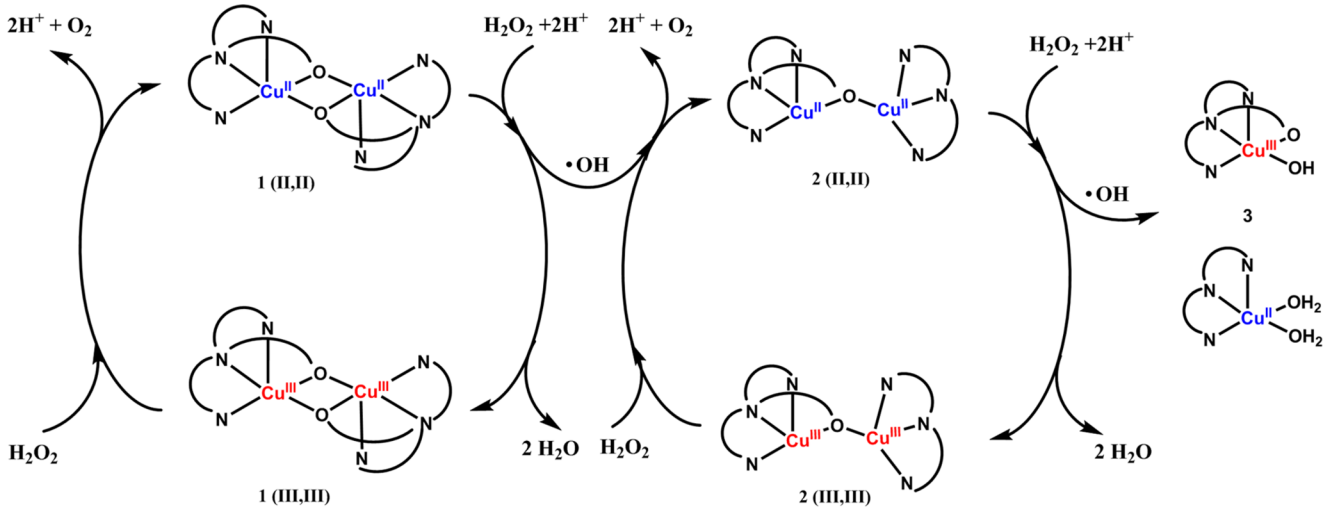

presence of NaBr shows a saturation trend (Figure S66), and it is explained by an increased stability of the active catalyst, due to the switching off of radical side-reactions by added NaBr. The copper-catalyzed cycle for H_2O_2 dismutation by **1** is proposed in Scheme 3, where (i) dinuclear **1** and **2** are the active catalysts, cycling between the $Cu_2^{III,III} \rightarrow Cu_2^{II,II}$ redox states, and (ii) radical pathways are responsible for a parallel catalyst degradation route, **1** → **2** → **3**, that turns out to be mitigated by addition of bromide salts or in saline buffers as KH.

A similar NaBr effect has also been registered in the reactions catalyzed by $\mathbf{Cu_2L^2_2}$ and $\mathbf{Cu_2L^3_2}$, with oxygen evolution rates that increase steadily reaching a H_2O_2 conversion >95% (Figures S67 and S68 and Table S4). ESI-MS analysis also confirms that $\mathbf{Cu_2L^2_2}$ and $\mathbf{Cu_2L^3_2}$ undergo a similar oxidative degradation when reacted with H_2O_2. Indeed, copper monomers are observed at $m/z < 500$ that are ascribed to dimer dissociation and ligand oxidation at the benzylic methylene and at the secondary amine site (Figures S45, S46, and S51 and Table S3).[38]

The stepwise evolution of the dimeric copper-core under oxygenic turnover (**1** → **2** → **3**, Scheme 3) has been further addressed by X-band EPR analysis at 50 K. To this aim, the reaction solution, after addition of H_2O_2, was quenched under liquid nitrogen at definite time intervals, and EPR spectra were registered over time. Representative experiments preformed for $\mathbf{Cu_2L^1_2}$ are reported in Figure 4, both in the absence and in the presence of the NaBr additive.[39]

Low-temperature EPR analysis is instrumental to investigate the magnetic properties of Cu(II) d^9-complexes, as a function of their coordination geometry, the symmetry of ligation, the bond distances, and the resulting Cu(II)−Cu(II) interactions. In particular, a significant modification of the EPR features is envisaged along the reaction progress, whereby the bis-μ-phenolate, Cu_2O_2 core of **1** is expected to open up to a more open, mono-μ-phenolate dimer **2**, and eventually leading to Cu(II) monomers **3**.

In all cases, the starting dimers **1** turn out to be EPR silent (X band, 50 K; Figure 4 and Figure S77) which indicates a diamagnetic ($S = 0$) state, due to a strong antiferromagnetic coupling between the copper centers in the Cu_2O_2-core. Soon after the addition of H_2O_2 (<10 min), the EPR spectra show the formation of a copper signal, that gradually evolves from an

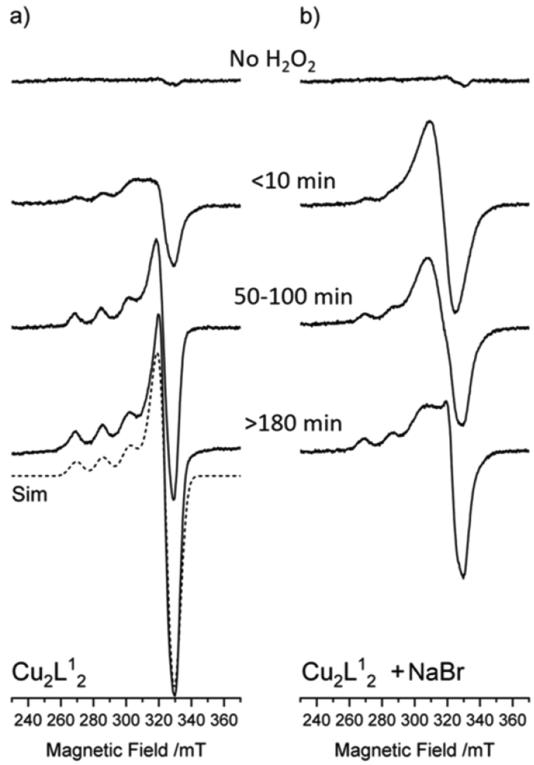

Figure 4. (a) X-band EPR spectra at 50 K of $\mathbf{Cu_2L^1_2}$ (200 μM) before and after the addition of H_2O_2 (30 mM) in BBS (50 mM pH = 7.8). EPR analysis was performed on frozen aliquots of the reaction mixture, sampled at the indicated time. The monomer simulated spectrum is reported with a dashed line. (b) As above but with NaBr (50 mM), added before H_2O_2. The spectra are shown with their original intensity.

initial broad line shape to a narrow one typical of the monomeric copper complex (Figure 4a). An analogous trend is also registered in the presence of added bromide, albeit with a slower kinetics (Figure 4b). In both cases, the amount of paramagnetic species, calculated from the double integral of the spectra, steadily increases with time, confirming that the initial diamagnetic complex gradually breaks down into paramagnetic species.

https://dx.doi.org/10.1021/acscatal.0c01955
ACS Catal. 2020, 10, 7295−7306

The broad EPR signal, dominant at early stages, shows no resolved g and hyperfine tensor features and likely arises from a weak coupling between the two copper centers via dipole−dipole and exchange interactions. We ascribe this signature to a modification of the copper-core, where the spin−spin coupling is responsible for the broadening of the EPR features, but it is not strong enough to give rise to a triplet state ($S = 1$), which is consistent with the formation of paramagnetic "loose" dimers.[40] The EPR signals appearing at longer time intervals (>50 min) are typical of a monomeric $S = 1/2$ copper species with an expected four-line pattern in the $g_{\|}$ region consistent with hyperfine interaction with the Cu nucleus ($I = 3/2$). The powder EPR spectrum of the monomer has been simulated with an axial g and A tensors ($g_{\|} = 2.273$, $g_{\perp} = 2.059$; $A_{\|} = 500$ MHz, $A_{\perp} = 5$ MHz; Figure 4a, dashed line), using the Easyspin simulation program.[41] The magnetic tensors are consistent with a distorted octahedral geometry imparted by the multidentate ligand environment.[42]

An analogous behavior is observed for $\mathbf{Cu_2L^2_2}$ and $\mathbf{Cu_2L^3_2}$ (Figure S76); therefore, the EPR analysis and the timeline of the registered spectral evolution complement the ESI-MS evidence, confirming the stepwise transformation of the pristine copper dimers, **1**, under the turnover regime, that leads to "loose" dimers, **2**, up to the catalytically inactive monomers, **3**.We can thus propose the catalytic cycle reported in Scheme 3 that occurs along three reaction pathways where the copper dimers **1** and **2** are all active catalysts: namely, (i) the reductive half-reaction of H_2O_2 dismutation in which the fully reduced Cu(II,II) is responsible for a two-electron/two proton transfer that cleaves the O−O bond and releases water, while being oxidized to the Cu(III,III) state; (ii) the oxidative half-reaction of H_2O_2 dismutation in which the fully oxidized Cu(III,III)-core is responsible for a two-electron/two-proton oxidation, liberating O_2, while restoring the reduced copper-core to close the catalytic cycle; and (iii) a Fenton-like radical mechanism that originates from the Cu(II,II)-core, by single electron transfer, that cleaves the O−O bond and generates the highly reactive •OH species. This latter pathway is responsible for ligand degradation eventually leading to the inactive copper monomers, **3**.

In this scheme, the dismutation catalysis by the pristine dimers, **1**, turns out to be the dominant pathway at the early reaction stage (<20 min) as indicated by ESI and EPR evidence on copper speciation (Figure 3b, black line; and Figure 4a). At intermediate times (<100 min), the steady accumulation of dimers **2** in solution (Figure 3b, red-line; and Figure 4a), resulting from the homolytic side-reaction, does not slow down the H_2O_2 catalytic dismutation. This observation supports a bioinspired catalase mechanism, where the phenolate-bridged dimetal core serves as a "storage" station for electrons and protons used by the catalytic manifold, cycling between the Cu(II,II) and Cu(III,III) redox states.[43] Indeed, the catalytic dismutation of H_2O_2 is switched off when copper monomers are prevalent at longer reaction times (>150 min) as indicated by the combined ESI and EPR evidence (Figure 3b, blue line; and Figure 4a). Furthermore, the increased activity and stability observed upon addition of a radical scavenger like bromide (Figures 3c and 4b) are explained by the suppression of monomer formation along the reaction progress (compare blue traces in Figure 3b,c, and EPR signals a and b in Figure 4). It is important to underline that, due to the high complexity of the process and the presence of multiple side reactions, alternative or parallel pathways cannot be excluded.

In this scenario, H_2O_2 coordination to one copper center, followed by the opening of one phenol bridge and the structural rearrangement of the complex, is likely responsible for the lag-phase especially evident in the oxygen evolution kinetics by $\mathbf{Cu_2L^1_2}$ leading to a structure similar to a recently reported di-Mn(II) catalase mimicry.[7a]

To highlight the privileged CAT-like reactivity of the Cu_2(II)-core, we have addressed the kinetic relevance of possible competitive pro-oxidant pathways triggered by H_2O_2. As a representative case, the antioxidant versus pro-oxidant capacity of $\mathbf{Cu_2L^1_2}$ has been evaluated by considering the catalytic bleaching of morin, generally used as the molecular probe for peroxidase screening (Scheme S1).[44−47] The oxidative degradation of morin (0.12 mM) catalyzed by $\mathbf{Cu_2L^1_2}$ (50 μM) in the presence of H_2O_2 (10−30 mM in BBS buffer 50 mM, pH = 7.8, Figures S78−S80) is conveniently monitored via UV−vis spectroscopy, by registering the absorbance depletion at 390 nm over a time-range superimposable to the oxygen evolution kinetics. The rate of morin bleaching by $\mathbf{Cu_2L^1_2}$ varies linearly with H_2O_2 concentration, yielding a second-order rate constants, $k_b = 6.1 \times 10^{-4}$ M^{-1} s^{-1}, that is orders of magnitude lower than the $k_{H_2O_2}$ associated with the catalase-like activity of the copper complex (cf. Table 1; and Table S6 and Figure S80). The relative impact of the antioxidant versus the pro-oxidant performance of $\mathbf{Cu_2L^1_2}$ can thus be evaluated on the basis of the so-called "protection" factor $p = k_{H_2O_2}/k_b$, calculated as the ratio between the rate constants associated, respectively, with H_2O_2 dismutation and catalytic bleaching.[7a,48] As expected, the value of $p = 377$ obtained for $\mathbf{Cu_2L^1_2}$ confirms the prominent H_2O_2 dismutation activity by the dinuclear copper-core.[49,50]

CONCLUSIONS

Our results showcase the first example of a dinuclear Cu(II)-core exhibiting a dual SOD/CAT-like activity, in water under physiological pH. A tailored modification of the dinucleating ligand HL^1 has been instrumental to optimize kinetics and performance of both SOD and CAT manifolds. Other N_3O-ligand sets in combination with copper were not reported to promote a dual antioxidant activity.[51] In particular, peak activities ($\log k_{cat}(O_2^{\bullet-}) = 7.55$ and $k_{H_2O_2}$ up to 0.66 M^{-1} s^{-1}) are obtained with an HL ligand featuring a secondary amine and a p-nitrophenolate residue as key stereoelectronic effectors within the $\mathbf{Cu_2L^3_2}$ coordination sphere. $\mathbf{Cu_2L^3_2}$ stands as the most efficient and unique Cu_2-based artificial SOD/CAT compared to literature benchmarks (Table 1).[8−10,24] The resulting structure−reactivity trend $\mathbf{Cu_2L^1_2} < \mathbf{Cu_2L^2_2} < \mathbf{Cu_2L^3_2}$ is supported by converging structural, electrochemical, and kinetics evidence, whereby the SOD and CAT manifold are, respectively, related to the $Cu_2^{II,II/I,I}$ and $Cu_2^{III,III/II,II}$ redox couples, mimicking the enzymatic mechanism. ESI-MS and EPR analysis of the time-dependent evolution of $\mathbf{Cu_2L^x_2}$ under oxygen evolution turnovers confirms the active role of the Cu_2-core for H_2O_2 dismutation, as monomeric fragments are found catalytically inactive. The prominent two-electron versus single-electron mechanism is also confirmed with radical scavenger probes, that turn out to favor the turnover efficiency, by depleting side ligand degradation pathways. While the peroxidase-like activity is often exhibited by artificial catalases,[45] a high pro-oxidant activity is a potential risk factor

https://dx.doi.org/10.1021/acscatal.0c01955
ACS Catal. 2020, 10, 7295−7306

for the intrinsic stability of the artificial SOD/CAT complex, as the metal first coordination sphere represents a proximal oxidation target. In this scenario, the pro-oxidant activity of the Cu_2-core is low compared to H_2O_2 dismutation, yielding a high protection factor, p = 377. In conclusion, copper-based artificial SOD/CAT can offer a valuable alternative to iron and manganese analogues, while unveiling the impact of the coordination environment for contrasting copper toxicity.[7,22,52] Further studies will be directed to address the mechanistic scenario vis-à-vis the proposed reaction manifold (Scheme 3).

■ ASSOCIATED CONTENT

Supporting Information

The Supporting Information is available free of charge at https://pubs.acs.org/doi/10.1021/acscatal.0c01955.

Synthesis and characterization data for all the copper complexes, X-ray structural information, electrochemical and kinetic studies (PDF)

Accession Codes

Crystallographic data for the reported structures have been deposited with the Cambridge Crystallographic Data Center (1564618; 1564619; 1564620) and can be obtained free of charge upon application to the CCDC, 12 Union Road, Cambridge CB2 1EZ, U.K. [Fax: (internat.) +44-1223/336-033; E-mail: deposit@ccdc.cam.ac.uk].

■ AUTHOR INFORMATION

Corresponding Author

Marcella Bonchio − *ITM-CNR and Department of Chemical Sciences, University of Padova, 35131 Padova, Italy;* orcid.org/0000-0002-7445-0296; Email: marcella.bonchio@unipd.it

Authors

Andrea Squarcina − *ITM-CNR and Department of Chemical Sciences, University of Padova, 35131 Padova, Italy;* orcid.org/0000-0003-1770-586X

Alice Santoro − *ITM-CNR and Department of Chemical Sciences, University of Padova, 35131 Padova, Italy*

Neal Hickey − *Department of Chemical and Pharmaceutical Sciences, University of Trieste, 34127 Trieste, Italy*

Rita De Zorzi − *Department of Chemical and Pharmaceutical Sciences, University of Trieste, 34127 Trieste, Italy*

Mauro Carraro − *ITM-CNR and Department of Chemical Sciences, University of Padova, 35131 Padova, Italy*

Silvano Geremia − *Department of Chemical and Pharmaceutical Sciences, University of Trieste, 34127 Trieste, Italy*

Marco Bortolus − *Department of Chemical Sciences, University of Padova, 35131 Padova, Italy;* orcid.org/0000-0002-6033-6521

Marilena Di Valentin − *Department of Chemical Sciences, University of Padova, 35131 Padova, Italy;* orcid.org/0000-0002-2915-8704

Complete contact information is available at: https://pubs.acs.org/10.1021/acscatal.0c01955

Notes

The authors declare no competing financial interest.

■ ACKNOWLEDGMENTS

CaRiPaRo Foundation, Starting Grants 2015 (AMYCORES), University of Padova (PRAT 2015 Prot. CPDA158234), MIUR PRIN (Prot. 2017PBXPN4), and the COST Action CM1205 (CARISMA) are gratefully acknowledged.

■ REFERENCES

(1) (a) Finkel, T.; Holbrook, N. J. Oxidants, Oxidative Stress and the Biology of Ageing. *Nature* **2000**, *408*, 239−247. (b) Cadenas, E.; Davis, K. J. A. Mitochondrial Free Radical Generation, Oxidative Stress, and Aging. *Free Radical Biol. Med.* **2000**, *29*, 222−230.

(2) (a) Zorov, D. B.; Juhaszova, M.; Sollott, S. J. Mitochondrial Reactive Oxygen Species (ROS) and ROS-Induced ROS Release. *Physiol. Rev.* **2014**, *94*, 909−950. (b) Signorella, S.; Hureau, C. Bioinspired Functional Mimics of the Manganese Catalases. *Coord. Chem. Rev.* **2012**, *256*, 1229−1245.

(3) (a) Eskici, G.; Axelsen, P. H. Copper and Oxidative Stress in the Pathogenesis of Alzheimer's Disease. *Biochemistry* **2012**, *51*, 6289−6311. (b) Hu, X.; Zhang, Q.; Wang, W.; Yuan, Z.; Zhu, X.; Chen, B.; Chen, X. Tripeptide GGH as the Inhibitor of Copper-Amyloid-β-Mediated Redox Reaction and Toxicity. *ACS Chem. Neurosci.* **2016**, *7*, 1255−1263. (c) Kenche, V.; Barnham, K. J. Alzheimer's Disease & Metals: Therapeutic Opportunities. *Br. J. Pharmacol.* **2011**, *163*, 211−219.

(4) (a) Michel, E.; Nauser, T.; Sutter, B.; Bounds, P. L.; Koppenol, W. H. Kinetics Properties of Cu,Zn-Superoxide Dismutase as a Function of Metal Content. *Arch. Biochem. Biophys.* **2005**, *439*, 234−240. (b) Goldstein, S.; Fridovich, I.; Czapski, G. Kinetic Properties of Cu,Zn-Superoxide Dismutase as a Function of Metal Content-Order Restored. *Free Radical Biol. Med.* **2006**, *41*, 937−941. (c) Ellerby, R. M.; Cabelli, D. E.; Graden, J. A.; Valentine, J. S. Copper−Zinc Superoxide Dismutase: Why not pH-Dependent? *J. Am. Chem. Soc.* **1996**, *118*, 6556−6561.

(5) Abreu, A.; Cabelli, D. E. Superoxide Dismutases a Review of the Metal-Associated Mechanistic Variations. *Biochim. Biophys. Acta, Proteins Proteomics* **2010**, *1804*, 263−274.

(6) (a) Beal, M. F.; Ferrante, R. J.; Browne, S. E.; Matthews, R. T.; Kowall, N. W.; Brown, R. H. Increased 3-Nitrotyrosine in Both Sporadic and Familial Amyotrophic Lateral Sclerosis. *Ann. Neurol.* **1997**, *42*, 644−654. (b) Shibata, N.; Hirano, A.; Kobayashi, M.; Sasaki, S.; Takeo, K.; Matsumoto, S.; Shiozawa, Z.; Komori, T.; Ikemoto, A.; Umahara, T.; Asayama, K. Cu/Zn Superoxide Dismutase-Like Immunoreactivity in Lewy Body-Like Inclusions of Sporadic Amyotrophic Lateral Sclerosis. *Neurosci. Lett.* **1994**, *179*, 149−152.

(7) (a) Squarcina, A.; Sorarù, A.; Rigodanza, F.; Carraro, M.; Brancatelli, G.; Carofiglio, T.; Geremia, S.; Larosa, V.; Morosinotto, T.; Bonchio, M. Merged Heme and Non-Heme Manganese Cofactors for a Dual Antioxidant Surveillance in Photosynthetic Organisms. *ACS Catal.* **2017**, *7*, 1971−1976. (b) Signorella, S.; Palopoli, C.; Ledesma, G. Rationally Designed Mimics of Antioxidant Manganoenzymes: Role of Structural Features in the Quest for Catalysts with Catalase and Superoxide Dismutase Activity. *Coord. Chem. Rev.* **2018**, *365*, 75−102. (c) Kubota, R.; Asayama, S.; Kawakami, H. Catalytic Antioxidants for Therapeutic Medicine. *J. Mater. Chem. B* **2019**, *7*, 3165−3191.

(8) (a) Saczewski, F.; Dziemidowicz-Borys, E.; Bednarski, P. J.; Gruunert, R.; Gdaniec, M.; Tabin, P. Synthesis, Crystal Structure and Biological Activities of Copper(II) Complexes with Chelating Bidentate 2-Substituted Benzimidazole Ligands. *J. Inorg. Biochem.* **2006**, *100*, 1389−1398. (b) Duracková, Z.; Labuda, J. Superoxide Dismutase Mimetic Activity of Macrocyclic Cu(II)-Tetraanhydroaminobenzaldehyde (TAAB) Complex. *J. Inorg. Biochem.* **1995**, *58*, 297−303. (c) Ohtsu, H.; Shimazaki, Y.; Odani, A.; Yamauchi, O.; Mori, W.; Itoh, S.; Fukuzumi, S. Synthesis and Characterization of Imidazolate-Bridged Dinuclear Complexes as Active Site Models of Cu,Zn-SOD. *J. Am. Chem. Soc.* **2000**, *122*, 5733−5741.

(9) (a) Cejudo-Marín, R.; Alzuet, G.; Ferrer, S.; Borrás, J. Functional Superoxide Dismutase Mimics. Structural Characterization and Magnetic Exchange Interactions of Copper(II)−N-Substituted Sulfonamide Dimer Complexes. *Inorg. Chem.* **2004**, *43*, 6805−6814. (b) Tabbi, G.; Driessen, W. L.; Reedijk, J.; Bonomo, R. P.; Veldman, N.; Spek, A. L. High Superoxide Dismutase Activity of a Novel, Intramolecularly Imidazolato-Bridged Asymmetric Dicopper(II) Species. Design, Synthesis, Structure, and Magnetism of Copper(II) Complexes with a Mixed Pyrazole−Imidazole Donor Set. *Inorg. Chem.* **1997**, *36*, 1168−1175.

(10) (a) Ramadan, A. M. E. Syntheses and Characterization of New Tetraazamacrocyclic Copper(II) Complexes as a Dual Functional Mimic Enzyme (Catalase and Superoxide Dismutase). *J. Coord. Chem.* **2012**, *65*, 1417−1433. (b) Devereux, M.; O'Shea, D.; Kellett, A.; McCann, M.; Walsh, M.; Egan, D.; Deegan, C.; Kedziora, K.; Rosair, G.; Müller-Bunz, H. Synthesis, X-ray Crystal Structures and Biomimetic and Anticancer Activities of Novel Copper(II)benzoate Complexes Incorporating 2-(4′-thiazolyl)benzimidazole (Thiabendazole), 2-(2-pyridyl)benzimidazole and 1,10-phenanthroline as Chelating Nitrogen Donor Ligands. *J. Inorg. Biochem.* **2007**, *101*, 881−892. (c) Pires dos Santos, M. L.; Faljoni-Alàrio, A.; Mangrich, A. S.; da Costa Ferreira, A. M. Antioxidant and Pro-Oxidant Properties of Some Di-Schiff Base Copper (II) Complexes. *J. Inorg. Biochem.* **1998**, *71*, 71−78. (d) Aliaga, M. E.; Andrade-Acuña, D.; López-Alarcóna, C.; Sandoval-Acuña, C.; Speisky, H. Cu (II)−Disulfide Complexes Display Simultaneous Superoxide Dismutase-and Catalase-like Activities. *J. Inorg. Biochem.* **2013**, *129*, 119−126. (e) Jezowska-Bojczuk, M.; Leśniak, W.; Bal, W.; Kozłowski, H.; Gatner, K.; Jezierski, A.; Sobczak, J.; Mangani, S.; Meyer-Klaucke, W. Molecular Mechanism of Hydrogen Peroxide Conversion and Activation by Cu(II)-Amikacin Complexes. *Chem. Res. Toxicol.* **2001**, *14* (10), 1353−1362.

(11) (a) Shank, M.; Barynin, V.; Dismukes, G. C. Protein Coordination to Manganese Determines the High Catalytic Rate of Dimanganese Catalases. Comparison to Functional Catalase Mimics. *Biochemistry* **1994**, *33*, 15433−15436. (b) Zheng, M.; Khangulov, S. V.; Dismukes, G. C.; Barynid, V. V. Electronic Structure of Dimanganese(II,III) and Dimanganese(III,IV) Complexes and Dimanganese Catalase Enzyme: a General EPR Spectral Simulation Approach. *Inorg. Chem.* **1994**, *33*, 382−387. (c) Wu, A. J.; Penner-Hahn, J. E.; Pecoraro, V. L. Structural, Spectroscopic, and Reactivity Models for the Manganese Catalases. *Chem. Rev.* **2004**, *104*, 903−938.

(12) (a) Kaizer, J.; Csonka, R.; Speier, G.; Giorgi, M.; Réglier, M. Synthesis, Structure and Catalase-Like Activity of New Dicopper(II) Complexes with Phenylglyoxylate and Benzoate Ligands. *J. Mol. Catal. A: Chem.* **2005**, *236*, 12−17. (b) Ray, A.; Rosair, G. M.; Pilet, G.; Dede, B.; Gómez-García, C. J.; Signorella, S.; Bellú, S.; Mitra, S. Preferential Azido Bridging Regulating the Structural Aspects in Cobalt(III) and Copper(II)−Schiff Base Complexes: Syntheses, Magnetostructural Correlations and Catalytic Studies. *Inorg. Chim. Acta* **2011**, *375*, 20−30. (c) Caglar, S.; Adıguzel, E.; Caglar, B.; Saykal, T.; Sahin, E.; Buyukgungor, O. Synthesis, Crystal Structure, Spectroscopic, Thermal, Catechol Oxidase and Catalase-Like Studies: New Copper(II) Complexes of 2-Benzoylbenzoate and 2-Pyridilpropanol Ligands. *Inorg. Chim. Acta* **2013**, *397*, 101−109.

(13) (a) Vicario, J.; Eelkema, R.; Browne, W. R.; Meetsma, A.; La Crois, R. M.; Feringa, B. L. Catalytic Molecular Motors: Fuelling Autonomous Movement by a Surface Bound Synthetic Manganese Catalase. *Chem. Commun.* **2005**, 3936−3938. (b) Tagliapietra, M.; Squarcina, A.; Hickey, N.; De Zorzi, R.; Geremia, S.; Sartorel, A.; Bonchio, M. Hydrogen Evolution by Fe^{III} Molecular Electrocatalysts Interconverting between Mono and Di-Nuclear Structures in Aqueous Phase. *ChemSusChem* **2017**, *10*, 4430.

(14) La Crois, R. M. *Manganese Complexes as Catalysts in Epoxidation Reactions A Ligand Approach*. PhD dissertation, University of Groningen, NL, 2000.

(15) (a) Deacon, G. B.; Phillips, R. J. Relationships between the Carbon-Oxygen Stretching Frequencies of Carboxylato Complexes and the Type of Carboxylate Coordination. *Coord. Chem. Rev.* **1980**, *33*, 227−250. (b) Nakamoto, K. *Infrared and Raman Spectra of Inorganic and Coordination Compounds*, 5th ed.; Wiley-Interscience: New York, 1997.

(16) Dimers fragmentation under ESI-MS analysis has been confirmed by ESI tandem mass analysis, leading to peaks observed at m/z = 367.1, 353.1, and 398.1, respectively, for $[CuL^1]^+$, $[CuL^2]^+$, and $[CuL^3]^+$ monomers.

(17) Zhang, P.; Shao, C.; Zhang, Z.; Zhang, M.; Mu, J.; Guoa, Z.; Liu, Y. In Situ Assembly of well-Dispersed Ag Nanoparticles (AgNPs) on Electrospun Carbon Nanofibers (CNFs) for Catalytic Reduction of 4-Nitrophenol. *Nanoscale* **2011**, *3*, 3357−3363.

(18) (a) Oliveri, V.; Puglisi, A.; Viale, M.; Aiello, C.; Sgarlata, C.; Vecchio, G.; Clarke, J.; Milton, J.; Spencer, J. New Cyclodextrin-Bearing 8-Hydroxyquinoline Ligands as Multifunctional Molecules. *Chem. - Eur. J.* **2013**, *19*, 13946−13955. (b) Amundsen, A. R.; Whelan, J.; Bosnich, B. Biological Analogs. Nature of the Binding Sites of Copper-Containing Proteins. *J. Am. Chem. Soc.* **1977**, *99*, 6730−6739.

(19) Despite that we did not observe any spectral evidence (UV−vis and EPR) for the formation of a Cu(II)-phenoxyl radical, its transient formation cannot be excluded under the turnover regime.

(20) Coggins, M. K.; Zhang, M.-T.; Chen, Z.; Song, N.; Meyer, T. J. Single-Site Copper(II) Water Oxidation Electrocatalysis: Rate Enhancements with HPO_4^{2-} as a Proton Acceptor at pH 8. *Angew. Chem., Int. Ed.* **2014**, *53*, 12226−12230.

(21) Hureau, C.; Anxolabéhère-Mallart, E.; Martine, N.; Gonnet, F.; Rivière, E.; Blondin, G. Synthesis, Structure and Characterisation of New Phenolato-Bridged Manganese Complexes $[L_2Mn_2]^{2+}$ − Formation by Ligand Oxidation in L_aH [L_aH = N-(2-hydroxybenzyl)-N,N′-bis (2-pyridylmethyl) ethane-1,2-diamine]. *Eur. J. Inorg. Chem.* **2002**, *2002*, 2710−2719.

(22) (a) Batinić-Haberle, I.; Rebouças, J. L. S.; Spasojević, I. Superoxide Dismutase Mimics: Chemistry, Pharmacology, and Therapeutic Potential. *Antioxid. Redox Signaling* **2010**, *13*, 877−918. (b) Batinic-Haberle, I.; Tovmasyan, A.; Spasojevic, I. An Educational Overview of the Chemistry, Biochemistry and Therapeutic Aspects of Mn Porphyrins-From Superoxide Dismutation to H_2O_2-Driven Pathways. *Redox Biol.* **2015**, *5*, 43−65.

(23) (a) Batinić-Haberle, I.; Spasojevic, I.; Hambright, P.; Benov, L.; Crumbliss, A. L.; Fridovich, I. Relationship among Redox Potentials, Proton Dissociation Constants of Pyrrolic Nitrogens, and in Vivo and in Vitro Superoxide Dismutating Activities of Manganese(III) and Iron(III) Water-Soluble Porphyrins. *Inorg. Chem.* **1999**, *38*, 4011−4022. (b) McCord, J. M.; Fridovich, I. Superoxide Dismutase an Enzymic Function for Erythrocuperin (Hemocuprein). *J. Biol. Chem.* **1969**, *244*, 6049−6055.

(24) (a) Jitsukawa, K.; Harata, M.; Arii, H.; Sakurai, H.; Masuda, H. SOD Activities of the Copper Complexes with Tripodal Polypyridylamine Ligands Having a Hydrogen Bonding Site. *Inorg. Chim. Acta* **2001**, *324*, 108−116. (b) Daier, V. A.; Rivière, E.; Mallet-Ladeira, S.; Moreno, D. M.; Hureau, C.; Signorella, S. R. Synthesis, Characterization and Activity of Imidazolate-Bridged and Schiff-Base Dinuclear Complexes as Models of Cu,Zn-SOD. A Comparative Study. *J. Inorg. Biochem.* **2016**, *163*, 162−175. (c) Kenkel, I.; Franke, A.; Dürr, M.; Zahl, A.; Dücker-Benfer, C.; Langer, J.; Filipović, M. R.; Yu, M.; Puchta, R.; Fiedler, S. R.; Shores, M. P.; Goldsmith, C. R.; Ivanović-Burmazović, I. Switching Between Inner- and Outer-Sphere PCET Mechanisms of Small-Molecule Activation: Superoxide Dismutation and Oxygen/Superoxide Reduction Reactivity Deriving from the Same Manganese Complex. *J. Am. Chem. Soc.* **2017**, *139*, 1472−1484.

(25) All attempts to isolate reduced mixed-valence species in the presence of superoxide and H_2O_2, either in organic solvent or in water media, were not successful even at low temperature (up to −80 °C). Moreover, the reaction between the ligand precursor and Cu(I) salts, even under N_2 atmosphere, leads to fast ligand degradation and to the deposition of metallic copper.

(26) (a) Kindermann, N.; Dechert, S.; Demeshko, S.; Meyer, F. Proton-Induced, Reversible Interconversion of a μ-1,2-Peroxo and a μ-1,1-Hydroperoxo Dicopper(II) Complex. *J. Am. Chem. Soc.* **2015**,

https://dx.doi.org/10.1021/acscatal.0c01955
ACS Catal. 2020, 10, 7295−7306

137, 8002−8005. (b) Dalle, K. E.; Gruene, T.; Dechert, S.; Demeshko, S.; Meyer, F. Weakly Coupled Biologically Relevant $Cu^{II}_2(\mu\text{-}\eta^1{:}\eta^1\text{-}O_2)$ cis-Peroxo Adduct that Binds Side-On to Additional Metal Ions. *J. Am. Chem. Soc.* **2014**, *136*, 7428−7434. (c) Peterson, R. L.; Ginsbach, J. W.; Cowley, R. E.; Qayyum, M. F.; Himes, R. A.; Siegler, M. A.; Moore, C. D.; Hedman, B.; Hodgson, K. O.; Fukuzumi, S.; Solomon, E. I.; Karlin, K. D. Stepwise Protonation and Electron-Transfer Reduction of a Primary Copper−Dioxygen Adduct. *J. Am. Chem. Soc.* **2013**, *135*, 16454−16467. (d) Cao, R.; Saracini, C.; Ginsbach, J. W.; Kieber-Emmons, M. T.; Siegler, M. A.; Solomon, E. I.; Fukuzumi, S.; Karlin, K. D. Peroxo and Superoxo Moieties Bound to Copper Ion: Electron-Transfer Equilibrium with a Small Reorganization Energy. *J. Am. Chem. Soc.* **2016**, *138*, 7055−7066. (e) Izzet, G.; Zeitouny, J.; Akdas-Killig, H.; Frapart, Y.; Ménage, S.; Douziech, B.; Jabin, I.; Le Mest, Y.; Reinaud, O. Dioxygen Activation at a Mononuclear Cu(I) Center Embedded in the Calix[6]arene-Tren Core. *J. Am. Chem. Soc.* **2008**, *130* (29), 9514−9523. (f) Cole, A. P.; Mahadevan, V.; Mirica, L. M.; Ottenwaelder, X.; Stack, T. D. P. Bis(μ-oxo)dicopper(III) Complexes of a Homologous Series of Simple Peralkylated 1,2-Diamines: Steric Modulation of Structure, Stability, and Reactivity. *Inorg. Chem.* **2005**, *44* (21), 7345−7364. (g) Pirovano, P.; Magherusan, A. M.; McGlynn, C.; Ure, A.; Lynes, A.; McDonald, A. R. Nucleophilic Reactivity of a Copper(II)−Superoxide Complex. *Angew. Chem., Int. Ed.* **2014**, *53* (23), 5946−5950. (h) Kim, S.; Ginsbach, J. W.; Lee, J. Y.; Peterson, R. L.; Liu, J. J.; Siegler, M. A.; Sarjeant, A. A.; Solomon, E. I.; Karlin, K. D. Amine Oxidative N-Dealkylation via Cupric Hydroperoxide Cu-OOH Homolytic Cleavage Followed by Site-Specific Fenton Chemistry. *J. Am. Chem. Soc.* **2015**, *137*, 2867−2874.

(27) (a) Noël, S.; Perez, F.; Pedersen, J. T.; Alies, B.; Ladeira, S.; Sayen, S.; Guillon, E.; Gras, E.; Hureau, C. A New Water-Soluble Cu(II) Chelator that Retrieves Cu from Cu(amyloid-β) Species, Stops Associated ROS Production and Prevents Cu(II)-Induced Aβ Aggregation. *J. Inorg. Biochem.* **2012**, *117*, 322−325. (b) Faller, P.; Hureau, C.; Berthoumieu, O. Role of Metal Ions in the Self-Assembly of the Alzheimer's Amyloid-β Peptide. *Inorg. Chem.* **2013**, *52*, 12193−12206. (c) Viles, H. J. Metal Ions and Amyloid Fiber Formation in Neurodegenerative Diseases. Copper, Zinc and Iron in Alzheimer's, Parkinson's and Prion Diseases. *Coord. Chem. Rev.* **2012**, *256*, 2271−2284.

(28) The rate of oxygen production with $\mathbf{Cu_2L^1_2}$ shows saturation behavior amenable with the Michaelis−Menten equation (Figure S69). However, the large excess of H_2O_2 required (>60 mM) leads to degradation of the complex (Figures S70−S74), releasing copper and leading to the formation of copper hydroxide and oxides. For this reason, the Michaelis−Menten constants cannot be extrapolated.

(29) Krebs, H. A.; Henseleit, K. Untersuchungen über die Harnstoffbildung im Tierkörper. *Hoppe-Seyler's Z. Physiol. Chem.* **1932**, *210*, 33−66.

(30) Perez-Benito, J. F. Reaction Pathways in the Decomposition of Hydrogen Peroxide Catalyzed by Copper(II). *J. Inorg. Biochem.* **2004**, *98*, 430−438.

(31) The control reaction performed with $\mathbf{Cu_2L^1_2}$ in phosphate buffer (20 mM, pH = 7.8) shows a lag phase increased up to 4 h (Figure S58).

(32) Vikse, K. L.; Ahmadi, Z.; Scott McIndoe, J. The Application of Electrospray Ionization Mass Spectrometry to Homogeneous Catalysis. *Coord. Chem. Rev.* **2014**, *279*, 96−114.

(33) Direct evidence of innersphere ligand oxidation is provided by a low intensity peak at m/z = 847.0, ascribed to $[\mathbf{Cu_2L^1L^{Ox}} + ClO_4]^+$ (see Figures S36 and S39).

(34) In the presence of ligand-free Cu^{2+}, under the same experimental conditions, a brown precipitate is immediately formed, and hydrogen peroxide decomposition occurs with a steady kinetics (Figure S60).

(35) (a) Fei, B. L.; Yan, Q. L.; Wang, J. H.; Liu, Q. B.; Long, J. Y.; Li, Y. G.; Shao, K. Z.; Su, Z. M.; Sun, W. Y. Green Oxidative Degradation of Methyl Orange with Copper(II) Schiff Base Complexes as Photo-Fenton-Like. *Z. Anorg. Allg. Chem.* **2014**, *640* (10), 2035−2040. (b) Cao, J.; Luo, B.; Lin, H.; Chen, S. Synthesis, Characterization and Photocatalytic Activity of AgBr/H_2WO_4 Composite Photocatalyst. *J. Mol. Catal. A: Chem.* **2011**, *344*, 138−144.

(36) Sustmann, R.; Korth, H.; Kobus, D.; Baute, J.; Seiffert, K.; Verheggen, E.; Bill, E.; Kirsch, M.; de Groot, H. Fe^{III} Complexes of 1,4,8,11-Tetraaza[14]annulenes as Catalase Mimics. *Inorg. Chem.* **2007**, *46* (26), 11416−11430.

(37) Liao, C. H.; Kang, S. F.; Wu, F. A. Hydroxyl Radical Scavenging Role of Chloride and Bicarbonate Ions in the H_2O_2/UV Process. *Chemosphere* **2001**, *44*, 1193−1200.

(38) (a) Xiao, Q.; Connell, T. U.; Cadusch, J. J.; Roberts, A.; Chesman, A. S. R.; Gómez, D. E Hot-Carrier Organic Synthesis via the Near-Perfect Absorption of Light. *ACS Catal.* **2018**, *8*, 10331−10339. (b) Chen, J.; Unjaroen, D.; Stepanovic, S.; van Dam, A.; Gruden, M.; Browne, W. R. Selective Photo-Induced Oxidation with O_2 of a Non-Heme Iron(III) Complex to a Bis(imine-pyridyl)iron(II) Complex. *Inorg. Chem.* **2018**, *57*, 4510−4515. (c) Wegeberg, C.; Fernández-Alvarez, V. M.; de Aguirre, A.; Frandsen, C.; Browne, W. R.; Maseras, F.; McKenzie, C. J. Photoinduced O_2-Dependent Stepwise Oxidative Deglycination of a Nonheme Iron(III) Complex. *J. Am. Chem. Soc.* **2018**, *140*, 14150−14160.

(39) Similar experiments were performed with $\mathbf{Cu_2L^2_2}$ and $\mathbf{Cu_2L^3_2}$ catalysts, sampled at shorter time intervals, according to the fast reaction kinetics (Figure S76).

(40) (a) Toyama, N.; Asano-Someda, M.; Kaizu, Y. EPR Spectra of Gable-Type Copper(II) Porphyrin Dimers in Fluid Solution: Extraction of Exchange Interaction in Weakly Coupled Doublet Pairs. *Mol. Phys.* **2003**, *101* (6), 733−742. (b) Jezierska, J.; Kokozay, V.; Ozarowski, A. EPR Studies of Spin−Spin Interactions between Cu(II) Centers in Dimeric, Hexameric and Homo- and Heteronuclear Tetrameric Complexes. *Res. Chem. Intermed.* **2007**, *33* (8−9), 901−914.

(41) Stoll, S.; Schweiger, A. EasySpin, a Comprehensive Software Package for Spectral Simulation and Analysis in EPR. *J. Magn. Reson.* **2006**, *178*, 42−55.

(42) Hathaway, B. J.; Billing, D. E. I The Electronic Properties and Stereochemistry of Mono-Nuclear Complexes of the Copper(II) Ion. *Coord. Chem. Rev.* **1970**, *5* (2), 143−207.

(43) Whittaker, J. W. Non-Heme Manganese Catalase − The 'Other' Catalase. *Arch. Biochem. Biophys.* **2012**, *525*, 111−120.

(44) Pelletier, H.; Kraut, J. Crystal Structure of a Complex between Electron Transfer Partners, Cytochrome c Peroxidase and Cytochrome c. *Science* **1992**, *258*, 1748−1755.

(45) (a) Wieprecht, T.; Xia, J.; Heinz, U.; Dannacher, J.; Sclingloff, G. Novel Terpyridine-Manganese(II) Complexes and their Potential to Activate Hydrogen Peroxide. *J. Mol. Catal. A: Chem.* **2003**, *203*, 113−128. (b) Polzer, F.; Wunder, S.; Lu, Y.; Ballauff, M. Oxidation of an Organic Dye Catalyzed by MnO_x Nanoparticles. *J. Catal.* **2012**, *289*, 80−87.

(46) Pap, J. S.; Kripli, B.; Bors, I.; Bogáth, D.; Giorgi, M.; Kaizer, J.; Speier, G. Transition Metal Complexes Bearing Flexible N_3 or N_3O Donor Ligands: Reactivity Toward Superoxide Radical Anion and Hydrogen Peroxide. *J. Inorg. Biochem.* **2012**, *117*, 60−70.

(47) (a) Wieprecht, T.; Heinz, U.; Xia, J.; Sclingloff, G.; Dannacher, J. Terpyridine-Manganese Complexes: A New Class of Bleach Catalysts for Detergent Applications. *J. Surfactants Deterg.* **2004**, *7*, 59−66. (b) Abdolahzadeh, S.; Boyle, N. M.; Hage, R.; de Boer, J. W.; Browne, W. R. Metal-Catalyzed Photooxidation of Flavones in Aqueous Media. *Eur. J. Inorg. Chem.* **2018**, *2018*, 2621−2630.

(48) The protection factor p was calculated as the ratio between $k_{H_2O_2}/k_b$ obtained by the reported $p = k_{cat}/(K_M k_b)$ equation where $k_{cat}/K_M = k_{H_2O_2}$.

(49) UV−vis monitoring of morin bleaching by the best performing $\mathbf{Cu_2L^3_2}$ is hampered by spectral overlap; however, similar p factors can be expected considering the enhanced $k_{H_2O_2}$ and TON values leveling off at ca. 40% O_2 yield (Table 1, Figure 1), thus indicating a similar balance between catalase-like activity (antioxidant) and catalytic ligand oxidation (pro-oxidant).

https://dx.doi.org/10.1021/acscatal.0c01955
ACS Catal. 2020, 10, 7295−7306

(50) For the sake of comparison, the reference mononuclear copper complex, Cu(PBMPA), is characterized by a $p \approx 10^{-4}$, thus showing a reversed antioxidant response (cf. Table 1 and Table S6). The low p value might arise from prevailing single-electron transfer mechanisms, with the formation of radical species.
(51) (a) Ribeiro, T. P.; Fernandes, C.; Melo, K. V.; Ferreira, S. S.; Lessa, J. A.; Franco, R. W. A.; Schenk, G.; Pereira, M. D.; Horn, A., Jr. Iron, Copper, and Manganese Complexes with in Vitro Superoxide Dismutase and/or Catalase Activities that Keep Saccharomyces Cerevisiae Cells Alive under Severe Oxidative Stress. *Free Radical Biol. Med.* **2015**, *80*, 67−76. (b) MacLean, L.; Karcz, D.; Jenkins, H.; McClean, S.; Devereux, M.; Howe, O.; Pereira, M. D.; May, N. V.; Enyedy, E. A.; Creaven, B. S. Copper(II) Complexes of Coumarin-Derived Schiff Base Ligands: Pro- or Antioxidant Activity in MCF-7 Cells? *J. Inorg. Biochem.* **2019**, *197*, 110702.
(52) (a) Batinic-Haberle, I.; Rajic, Z.; Tovmasyan, A.; Reboucas, J. S.; Ye, X.; Leong, K. W.; Dewhirst, M. W.; Vujaskovic, Z.; Benov, L.; Spasojevic, I. Diverse Functions of Cationic Mn(III) N-Substituted Pyridylporphyrins, Recognized as SOD Mimics. *Free Radical Biol. Med.* **2011**, *51* (5), 1035−1053. (b) Tovmasyan, A.; Maia, C. G. C.; Weitner, T.; Carballal, S.; Sampaio, R. S.; Lieb, D.; Ghazaryan, R.; Ivanovic-Burmazovic, I.; Ferrer-Sueta, G.; Radi, R.; Reboucas, J. S.; Spasojevic, I.; Benov, L.; Batinic-Haberle, I. A Comprehensive Evaluation of Catalase-Like Activity of Different Classes of Redox-Active Therapeutics. *Free Radical Biol. Med.* **2015**, *86*, 308−321.

https://dx.doi.org/10.1021/acscatal.0c01955
ACS Catal. 2020, 10, 7295−7306